

THE IMPACT OF FINITE SPAN AND WING-TIP VORTICES ON A TURBULENT NACA0012 WING

Siavash Toosi

Institute of Fluid Mechanics (LSTM)
Friedrich-Alexander-Universität (FAU) Erlangen-Nürnberg
Cauerstr. 4, 91058 Erlangen, Germany
siavash.toosi@fau.de

Adam Peplinski

FLOW
KTH Royal Institute of Technology
Osquars Backe 18, 11428 Stockholm, Sweden
adam@mech.kth.se

Philipp Schlatter

Institute of Fluid Mechanics (LSTM)
Friedrich-Alexander-Universität (FAU) Erlangen-Nürnberg
Cauerstr. 4, 91058 Erlangen, Germany
philipp.schlatter@fau.de

Ricardo Vinuesa

FLOW
KTH Royal Institute of Technology
Osquars Backe 18, 11428 Stockholm, Sweden
rvinuesa@mech.kth.se

ABSTRACT

High-fidelity simulations were conducted to investigate the turbulent boundary layers around a finite-span NACA0012 wing with rounded wing-tip geometry at a chord-based Reynolds number of $Re_c = 200000$ and various angles of attack up to 10° . This study aims at discerning the differences between the boundary layers on the finite-span wing and those on infinite-span wings at equivalent angles of attack. After excluding effects from the reduced effective angle of attack due to the induced velocity by the wing-tip vortex and other more localized three-dimensional effects (such as skewed velocity profiles), it was observed that the finite-span boundary layers exhibit a lower near-wall peak in their streamwise Reynolds stress profiles and a higher turbulence level near the boundary layer edge, particularly in regions closer to the wing tip. These discrepancies are explained by variations in adverse pressure gradient levels across the span, differences in flow history in the wall-normal direction caused by the skewed velocity profiles, and the variable boundary layer thickness caused by vortex formation and other finite-span effects. The primary focus of this study is on the turbulent boundary layers, with other aspects of the flow reserved for future investigations.

INTRODUCTION

The pressure difference between the suction and pressure sides of a finite-span wing results in the formation of wing-tip vortices. These vortices significantly influence the flow by inducing a downwash on the wing (i.e., an induced inviscid velocity oriented downwards relative to the free-stream; cf. Houghton *et al.*, 2013, and references therein). This phenomenon alters the free-stream direction by inducing a downward velocity component proportional to the vortex strength and inversely proportional to the distance from its core (governed by the Biot-Savart law), thereby reducing the wing effective angle of attack over the entire span. Since the magnitude of this induced downwash diminishes with increasing distance from the vortex core, different spanwise locations on the wing experience varied free-stream directions, resulting in a non-uniform spanwise pressure distribution. This causes a span-

wise pressure gradient, varying across both chord and span, and induces skewness in the velocity profile (cf. the review by Devenport & Lowe, 2022, and references therein). These have secondary implications on the turbulent boundary layers.

The primary objective of this study is to explore the flow near the wing, focusing on how the turbulent boundary layers are influenced by the presence of the wing-tip vortex and its induced three-dimensionality. The focus is on the differences between the finite- and infinite-span wings; thus, common behaviors such as the response to favorable and adverse pressure gradients are excluded from this study. More details about such effects can be found in works such as Spalart & Watmuff (1993); Perry *et al.* (2002); Bobke *et al.* (2017); Vinuesa *et al.* (2018); Gibis *et al.* (2019); Pozuelo *et al.* (2022). Furthermore, we limit our scope to the regions of the wing that are not dominated by wing-tip vortices or trailing edge effects.

High-fidelity simulations are employed to distinguish behaviors in finite-span wings that are absent in their infinite-span counterparts under similar configurations and effective angles of attack. The simulated wings have a symmetric NACA0012 profile and rounded wing-tip geometry. We study free-flight conditions at several angles of attack with a chord-based Reynolds number of $Re_c = U_\infty c / \nu = 200000$, where U_∞ denotes the free-stream velocity, c the chord length, and ν the kinematic viscosity.

NUMERICAL SETUP

The incompressible Navier–Stokes equations are spatially discretized and integrated over time using the high-order solver Nek5000 (Fischer *et al.*, 2010), which features adaptive mesh refinement (AMR) capabilities developed at KTH (Peplinski *et al.*, 2018; Offermans *et al.*, 2020; Tanarro *et al.*, 2020). The velocity field is approximated using polynomials of order $p = 7$, with dealiasing of the nonlinear convective term. The velocity–pressure coupling follows the $P_N - P_{N-2}$ formulation. Time integration is achieved through an implicit third-order backward differentiation scheme for viscous terms and an explicit third-order extrapolation for the nonlinear terms.

Table 1. Grids used in the study. P- α denotes periodic wings and RWT- α refers to finite-span wings. N_{GLL} is the total number of Gauss–Lobatto–Legendre (GLL) points. Δ values represent mean resolution calculated as element size over polynomial order, and $\delta_{1y_{\text{BL}}}$ is the distance from the wall of the first off-wall GLL point. Boundary layer resolutions, Δ^*_{BL} , are scaled by the viscous length δ_ν , while wake resolutions are normalized using the Kolmogorov scale, η .

Case	α	N_{GLL}	$(\Delta^*_{\text{BL}}, \delta_{1y_{\text{BL}}}, \Delta^*_{\text{BL}})$	$(\Delta x, \Delta y, \Delta z)/\eta$
P-0	0°	376×10^6	(10.3,0.72,8.7)	(5.8,3.6,3.7)
P-2	2°	383×10^6	(10.3,0.71,8.7)	(5.8,3.5,3.8)
P-5	5°	376×10^6	(10.5,0.73,8.5)	(5.2,3.2,3.3)
P-10	10°	438×10^6	(12.0,0.80,9.0)	(6.1,3.8,4.0)
RWT-0	0°	952×10^6	(11.4,0.70,6.9)	(5.5,2.6,1.7)
RWT-5	5°	1.56×10^9	(10.6,0.75,6.0)	(5.7,2.8,1.7)
RWT-10	10°	2.16×10^9	(10.6,0.80,5.4)	(5.6,3.0,1.8)

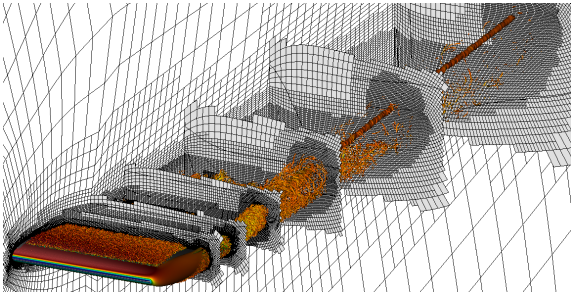


Figure 1. The grid used in RWT-10 as an example of the grids used in this study with instantaneous vortical structures represented by isosurfaces of $\lambda_2 c^2/U_\infty^2 = -100$ and colored by streamwise velocity, ranging from low (blue) to high (red), for visual reference.

This study encompasses seven configurations: four periodic (infinite-span) wing sections at angles $\alpha = 0^\circ, 2^\circ, 5^\circ,$ and 10° , and three finite-span wings at angles $\alpha = 0^\circ, 5^\circ,$ and 10° . Each wing maintains a non-tapered, non-swept planform without dihedral angles or twists. The three-dimensional wings feature an aspect ratio of 1.5 with rounded wing-tip geometry. Turbulence is induced via tripping of the boundary layers on both the suction and pressure sides in every case, and a symmetry boundary condition is enforced at the wing root.

The production grids are derived from an initial grid, refined iteratively using the solution-based spectral error indicator for turbulent flows, as outlined by Mavriplis (1990). Refinement is facilitated by manual interventions, such as designating wall elements for refinement. Table 1 presents a summary of the characteristics for the production grids used, indicating that their resolutions are close to those required for direct numerical simulation (DNS). An illustration of the grids used in this study is provided in Figure 1 using the example of RWT-10 with 4.23 million spectral elements.

Flow transients are removed both during the grid-adaptation stage and after reaching the production grid. Following the removal of these transients, solution statistics are collected over extended periods to ensure robustness: $5c/U_\infty$ for the periodic configurations (P-0, P-2, P-5, P-10), approximately $8c/U_\infty$ for RWT-0 and RWT-10, and an extended period of $23.2c/U_\infty$ for RWT-5. The averaging times for RWT-0 (which allows for averaging along the symmetric y -direction) and RWT-5 are similar in terms of the eddy turnover time—

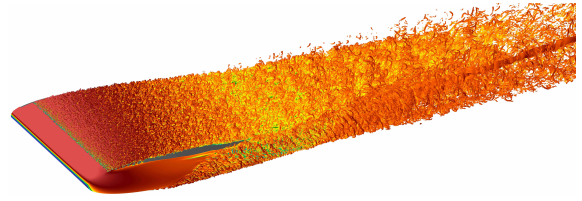


Figure 2. The instantaneous flow around the finite-span wing RWT-10. Plots show the instantaneous vortical structures, visualized by iso-surfaces of $\lambda_2 c^2/U_\infty^2 = -100$ colored by streamwise velocity from $-0.3U_\infty$ (blue) to $1.3U_\infty$ (red). The wing surface is shown in light grey.

defined based on the boundary layer thickness and friction velocity, δ_{99}/u_τ (Kim *et al.*, 1987)—which represents the most relevant timescale for the studied quantities. However, RWT-10 has a shorter integration period due to constraints on computational resources.

Statistics are collected on the fly at a sampling rate higher than the flow’s highest frequency, determined by the viscous timescale ν/u_τ^2 . For the periodic cases, which exhibit homogeneity in the spanwise direction, an ensemble average is also performed across this direction. Similarly, the RWT configurations (RWT-0, RWT-5, and RWT-10) benefit from the application of a wide Gaussian filter with an adjustable width tailored to the specific flow physics, facilitating a smoother and more accurate convergence of solution statistics. More details about the filtering procedure can be found in Toosi *et al.* (2024).

To ascertain the reliability of the statistical data, the complete record for each configuration is segmented into four equal batches. These batches are then used to compute the confidence intervals for each quantity of interest using the non-overlapping batch method (cf. Conway, 1963). The calculated confidence intervals are small compared to the observed differences between the finite- and infinite-span wings for all quantities of interest here, and are thus not plotted.

RESULTS AND DISCUSSIONS

The instantaneous flow field

The flow around the RWT-10 configuration is depicted in Figure 2, which illustrates the instantaneous vortical structures of the flow using the λ_2 visualization method proposed by Jeong & Hussain (1995). This visualization captures the turbulent boundary layer along the wing, the turbulent wake, and the prominent wing-tip vortex. This vortex appears as a cylindrical shape embedded within turbulent structures, initiating near the wing tip and maintaining coherence well downstream, covering the entire field of view in Figure 2. Notably, such a wing-tip vortex is only observable in configurations that generate lift, such as RWT-5 and RWT-10, and is absent in the RWT-0 configuration. The relatively low friction Reynolds number of the flow ($200 \lesssim Re_\tau \lesssim 300$) is apparent from the hairpin-dominated structure of the turbulent boundary layers (cf. Eitel-Amor *et al.*, 2015). Additionally, the tripping line spans the entire wing from root to tip, excluding the tip itself, resulting in laminar flow characteristics near the wing tip and a distinct laminar-turbulent interface at the spanwise end of the tripping line.

The impact of change in the effective angle of attack

The primary influence of wing-tip vortices is the induced downwash over the wing, altering the effective angle of attack, denoted as α_{eff} . Changes in α_{eff} lead to variations in the pressure distribution across the wing surface, thereby influencing the streamwise pressure gradients that the boundary layer encounters. Figure 3 offers a comparative analysis of the boundary layer thickness, δ_{99} , and the streamwise Clauser pressure gradient parameter β_{xBL} (Clauser, 1954, 1956) across all wings involved in this study. It is noteworthy that the boundary layers on finite-span wings exhibit similarities with those on periodic wings when compared at the same effective, rather than geometric, angle of attack. In order to eliminate these inviscid effects from our analysis, in the rest of this study, we compare finite- and infinite-span wings at similar α_{eff} .

The skewed velocity profiles, the collateral region near the wall, and rotation into wall-shear coordinates

The non-uniform pressure distribution along the span creates a spanwise pressure gradient on the wings. The combination of the nearly constant pressure gradient across the boundary layer thickness δ_{99} and the variations in flow momentum as a function of wall normal distance lead to a variable deflection angle of the flow. This skewness introduces additional shear components in the wall-normal direction, contributing to non-zero production terms for Reynolds stresses. As depicted by the mean streamlines in Figure 4 (a), these variations are more pronounced near the tip and diminish towards the root. However, Figure 4 (b) shows that γ_{stream} is relatively constant in the near-wall region, particularly for $y^+ \leq 30$, a region termed the collateral region (cf. Devenport & Lowe, 2022, and references therein). This constancy simplifies subsequent analyses; specifically, in a coordinate system aligned with the wall shear (i.e., the wall projection of the streamlines), the additional shear components disappear for $y^+ \leq 30$. As Reynolds stresses are lower above this region, the flow characteristics resemble those of two-dimensional boundary layers. The comparisons of the next section are based on the Reynolds stress components in the wall-shear-aligned coordinate system.

Non-local finite-span effects

Two other notable effects are associated with the finite span of the wing and the three-dimensional flow field. These are the underlying contributors to the discussed behaviors and departures from the infinite-span boundary layers observed here.

Firstly, the formation of wing-tip vortices drives a flow acceleration from the pressure side towards the suction side, yielding a wall-normal velocity that varies along both the chord and the span. Notably, areas closer to the tip and nearer the leading edge, where the vortex formation initiates, exhibit increased positive (away from the wall) wall-normal velocities (and its wall-normal gradient). This variation influences the boundary layer development, where increased wall-normal velocities correlate with an increased boundary layer growth rate through the continuity equation. Consequently, δ_{99} exhibits a slight increase near the tip on the suction side, while the boundary layers on the pressure side appear thinner in these regions. This phenomenon is primarily attributed to inviscid effects.

Secondly, the variation in the deflection angle in the normal distance from the wall, as a consequence of a combina-

tion of viscous and inviscid effects, results in streamlines that converge from different spanwise positions along the wing. Given that the effective angle of attack and consequently the streamwise pressure gradients vary across spanwise locations, fluid particles at different wall-normal distances have been subjected to different flow histories. This influence intensifies near the wing tip, where both the deflection angle variation (as depicted in Figure 4 (b)) and the pressure gradient variations are more pronounced.

In this analysis, the boundary layers on finite-span wings are compared with those on infinite-span wings to characterize these effects. Equivalence between the finite and infinite-span wings is based on the similarity of local values for Re_τ and β_{x_τ} , as well as the similarity in their development histories achieved by matching their effective angles of attack.

The first trend observed in Figure ?? (a) is a decrease in the near-wall peak of R_{11}^+ in finite-span wings in comparison to periodic profiles with streamwise distance, which becomes more pronounced further downstream. This discrepancy primarily stems from a milder adverse pressure gradient encountered by the boundary layer near the wing tip. This condition is a direct consequence of the reduced effective angle of attack in that specific region.

Another trend evident in Figure 5 (a) is the elevated Reynolds stress levels in the outer region of the boundary layer, particularly near its edge. This increase is more pronounced in spanwise locations closer to the tip. Furthermore, this effect shows a growing spanwise influence downstream. This phenomenon is linked to the increased wall-normal velocity and its gradient near the wing tip. The augmented wall-normal velocity causes greater boundary layer growth and thickness, which manifests as increased Reynolds stress levels observable at farther distances from the wall. The spanwise variation in wall-normal velocity tends to diminish downstream. These observations indicate that the expanding spanwise influence of this effect is likely initiated by the upstream conditions of the boundary layer, its subsequent flow development towards the root, and the spanwise propagation of non-zero fluctuations due to mixing and transport processes.

At these low Reynolds numbers, the available development length for the boundary layers, proportional to c/δ_{99} , is considerably lower than what is required to achieve equilibrium. This results in a transient response from the boundary layers to variations in their thickness, primarily manifesting as a displacement of the outer structures away from the wall. This shift propagates across the boundary layer thickness as it develops. This hypothesis is explored in Figure 5 (b), where the profiles from Figure 5 (a) are displayed in outer units. These profiles are juxtaposed with those from infinite-span wings at matched (Re_τ, β_{x_τ}) and matched δ_{99} conditions. A shift in the location of the outer structures away from the wall would be evidenced by a corresponding Reynolds stress profile near the boundary layer edge, which is the behavior indeed observed in Figure 5 (b). The extent of agreement in the wall-normal profiles around the boundary layer edge diminishes downstream, suggesting that this phenomenon is linked to the ongoing development of the boundary layers and their gradual response to the changes induced by increased thickness. Further exploration of the implications of this behavior is discussed subsequently.

The spanwise variation of R_{11}^+ is depicted in Figure 6 (a) and (b), revealing a noticeable reduction in the magnitude of the near-wall peak of the Reynolds stress, especially approaching the tip. This attenuation is influenced primarily by two mechanisms:

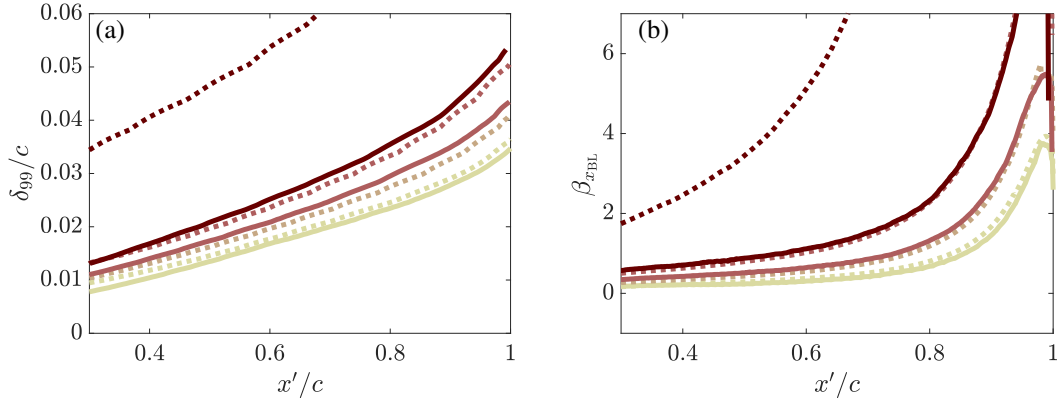


Figure 3. The impact of the effective angle of attack α_{eff} on boundary layers. Panels (a) and (b) show the change in boundary layer thickness δ_{99} and the streamwise Clauser pressure gradient parameter $\beta_{x\text{BL}}$ on the suction side of wings due to the change in α_{eff} . Different colors show different angles of attack from lightest to darkest corresponding to $\alpha = 0^\circ, 2^\circ, 5^\circ,$ and 10° , respectively. Solid lines correspond to finite-span wings, while dotted lines show the periodic cases.

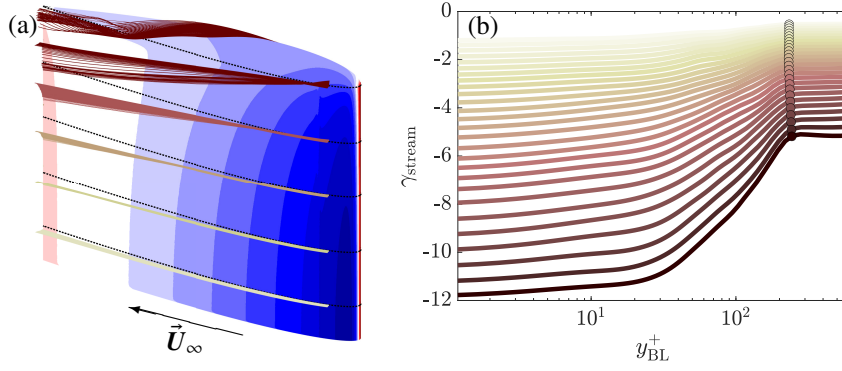


Figure 4. Deflection of the streamlines in RWT-5: (a) evolution of streamlines released downstream of the tripping line from equidistance locations in the spanwise location, (b) the deflection angle at a single streamwise location on the wing, with colors from light to dark showing different spanwise locations from the root to the tip. The contour plot on the wing surface in panel (a) shows the pressure coefficient c_p from -1 (dark blue) to $+1$ (dark red) in increments of 0.1 .

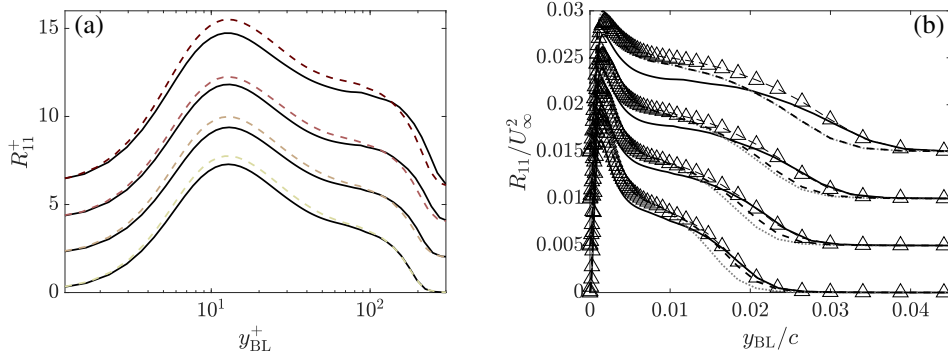


Figure 5. Variation of the (a) inner-scaled and (b) outer-scaled streamwise Reynolds stress with streamwise distance from the leading edge. Plotted profiles correspond to the evolution along streamlines released close to the tip. Profiles further downstream are shifted vertically by 2 units in panel (a) and by 0.005 units in panel (b) for visual clarity. The profiles are from RWT-5 (solid lines) and P-2 (dashed lines). All streamlines are released in the near-wall (approximately collateral) region.

Firstly, the effective angle of attack, which diminishes closer to the tip due to spanwise variation, results in milder adverse pressure gradients (characterized by lower $\beta_{x\tau}$ values). Consequently, there is a less pronounced increase in the inner-scaled Reynolds stress profiles and the turbulent kinetic energy that typically result from adverse pressure gradients.

This reduction in adverse effects leads to overall decreased inner-scaled Reynolds stress levels, manifesting as a reduced near-wall peak.

Secondly, the attenuation of the near-wall peak of R_{11}^+ is also attributed to the increased growth rate of the boundary layers near the tip. This growth leads to reduced production terms

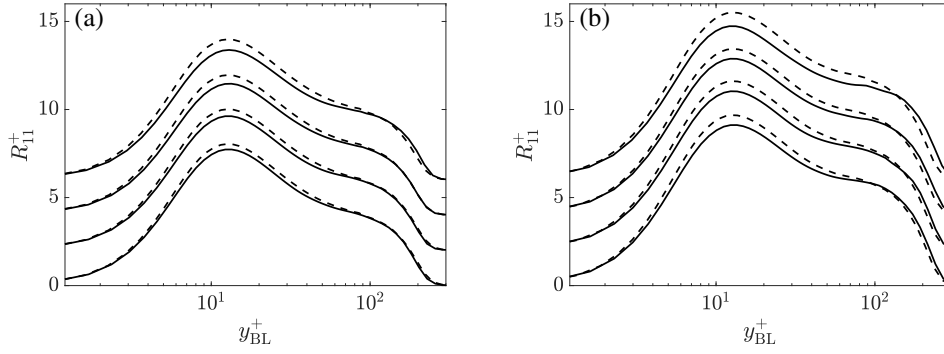


Figure 6. Variation of the inner-scaled Reynolds stress R_{11}^+ with spanwise distance from the root. Panels (a) and (b) correspond to distances of 70% and 90% from the leading edge, respectively. Profiles closer to the wing tip are shifted vertically by 2 units for visual clarity. The profiles are from RWT-5 (solid lines) and P-2 (dashed lines). All streamlines are released in the near-wall (approximately collateral) region.

near the wall due to decreased velocity gradients in the wall-normal direction as well as additional transport away from the wall. These dynamics collectively contribute to the reduction in the peak of R_{11}^+ profiles, thereby diminishing turbulence levels near the wall.

It is important to emphasize that the reference profiles used for comparisons in this section were selected to minimize potential discrepancies between the finite- and infinite-span wing profiles as much as possible. This approach ensures that the observed differences are primarily attributable to a few key mechanisms. However, this method also tends to mask some of the more significant discrepancies, potentially understating the real differences between the profiles. This is partially demonstrated in Figure 5 (b), which exhibits a larger variation in R_{11} profiles when only matching streamwise locations. Notably, at the spanwise location chosen for this figure, RWT-5 shows a reduced effective angle of attack of approximately 1° . A lower effective angle of attack generally results in thinner boundary layers and a more pronounced outer-scaled near-wall peak in R_{11} , suggesting that the actual difference between the finite- and infinite-span wings might be more substantial than what is portrayed in the figure.

SUMMARY AND CONCLUSIONS

High-fidelity simulations were conducted to investigate the turbulent boundary layers around a finite-span NACA0012 wing and to discern the differences between the boundary layers on the finite-span wing and those on infinite-span wings at equivalent angles of attack. A spanwise pressure gradient, a well-known inviscid effect, was present in all finite-span cases, including RWT-0, which does not generate lift. This pressure gradient caused the boundary layers to deflect towards the root on the suction side and towards the tip on the pressure side. The deflection angle varied across the span, chord, and in the wall-normal direction, reflecting a faster response from the low momentum fluid near the wall (see Devenport & Lowe, 2022, and references therein).

The variable deflection angle across the boundary-layer thickness means that fluid particles across a wall-normal line have converged from different spanwise locations and, due to the variable pressure gradient across the span, have different histories. Additionally, the increased wall-normal velocity along the span near the tip led to accelerated growth rates for the boundary layer farther from the root, each affecting the boundary layer in ways discussed. More details about the flow

and its physics is included in Toosi *et al.* (2024). Aspects of the flow other than those related to turbulent boundary layers are reserved for future investigations.

Interestingly, many attributes typically associated with three-dimensional turbulent boundary layers (summarized in Devenport & Lowe, 2022), such as a depressed wake in the mean velocity profile (cf. Spalart *et al.*, 2008), a reduction in Townsend’s structure parameter (cf. Littell & Eaton, 1994), or significant changes in the pressure-strain term (cf. Lozano-Durán *et al.*, 2020), were not observed in this study. This absence is likely due to the relatively weak variation of the deflection angle in the wall-normal direction and the gradual variation of this and other parameters along the streamlines, which allowed the boundary layers to approach their two-dimensional state.

In terms of modeling, the observed weak three-dimensionality in these boundary layers suggests that existing turbulence models may only require minor adaptations to account for these effects. Further research could explore the boundary layer behaviors in different wing configurations to better understand the scaling of these effects and refine predictive models accordingly.

ACKNOWLEDGEMENTS

This work was supported by the European Research Council (ERC), the Swedish Research Council (VR), and the Knut and Alice Wallenberg Foundation. RV acknowledges financial support from the ERC Grant No. “2021-CoG-101043998, DEEPCONTROL”.

We acknowledge PRACE for awarding us access to HAWK at GCS@HLRS, Germany. We also acknowledge the EuroHPC Joint Undertaking for awarding this project access to the EuroHPC supercomputer LUMI, hosted by CSC (Finland) and the LUMI consortium through EuroHPC Regular Access and EuroHPC Extreme Scale Access calls. Additional computations, data handling, and post-processing were enabled by resources provided by the National Academic Infrastructure for Supercomputing in Sweden (NAISS) and the Swedish National Infrastructure for Computing (SNIC) at PDC partially funded by the Swedish Research Council through grant agreements no. 2022-06725 and no. 2018-05973.

REFERENCES

- Bobke, A., Vinuesa, R., Örlü, R. & Schlatter, P. 2017 History effects and near equilibrium in adverse-pressure-gradient turbulent boundary layers. *J. Fluid Mech.* **820**, 667–692.
- Clauser, F. 1954 Turbulent boundary layers in adverse pressure gradients. *J. Aero. Sci.* **21** (2), 91–108.
- Clauser, F. 1956 The turbulent boundary layer. *Adv. Appl. Mech.* **4**, 1–51.
- Conway, R. W. 1963 Some tactical problems in digital simulation. *Manag. Sci.* **10** (1), 47–61.
- Devenport, W. & Lowe, K. 2022 Equilibrium and non-equilibrium turbulent boundary layers. *Prog. Aero. Sci.* **131**, 100807.
- Eitel-Amor, G., Örlü, R., Schlatter, P. & Flores, O. 2015 Hairpin vortices in turbulent boundary layers. *Phys. Fluids* **27**, 025108.
- Fischer, P., Lottes, J. & Kerkemeier, S. 2010 NEK5000: Open source spectral element CFD solver. Available at: <http://nek5000.mcs.anl.gov>.
- Gibis, T., Wenzel, C., Kloker, M. & Rist, U. 2019 Self-similar compressible turbulent boundary layers with pressure gradients. Part 2. Self-similarity analysis of the outer layer. *J. Fluid Mech.* **880**, 284–325.
- Houghton, E., Carpenter, P., Collicott, S. & Valentine, D. 2013 *Aerodynamics for Engineering Students*. Butterworth-Heinemann.
- Jeong, J. & Hussain, F. 1995 On the identification of a vortex. *J. Fluid Mech.* **285**, 69–94.
- Kim, J., Moin, P. & Moser, R. 1987 Turbulent statistics in fully developed channel flow at low Reynolds number. *J. Fluid Mech.* **177**, 133–166.
- Littell, H. & Eaton, J. 1994 Turbulence characteristics of the boundary layer on a rotating disk. *J. Fluid Mech.* **266**, 175–207.
- Lozano-Durán, A., Giometto, M., Park, G. I. & Moin, P. 2020 Non-equilibrium three-dimensional boundary layers at moderate Reynolds numbers. *J. Fluid Mech.* **883**, A20.
- Mavriplis, C. 1990 A posteriori error estimators for adaptive spectral element techniques. In *Proc. 8th GAMM-Conf. Num. Meth. Fluid Mech.*, pp. 333–342.
- Offermans, N., Peplinski, A., Marin, O. & Schlatter, P. 2020 Adaptive mesh refinement for steady flows in Nek5000. *Comps & Fluids* **197**, 104352.
- Peplinski, A., Offermans, N., Fischer, P. & Schlatter, P. 2018 Non-conforming elements in Nek5000: pressure preconditioning and parallel performance. In *Spectral and High Order Methods for Partial Differential Equations ICOSAHOM 2018*, pp. 599–609.
- Perry, A., Marusic, I. & Jones, M. 2002 On the streamwise evolution of turbulent boundary layers in arbitrary pressure gradients. *J. Fluid Mech.* **461**, 61–91.
- Pozuelo, R., Li, Q., Schlatter, P. & Vinuesa, R. 2022 An adverse-pressure-gradient turbulent boundary layer with nearly constant $\beta = 1.4$ up to $Re_\theta \approx 8700$. *J. Fluid Mech.* **939**, A34.
- Spalart, P., Coleman, G. N. & Johnstone, R. 2008 Direct numerical simulation of the Ekman layer: A step in Reynolds number, and cautious support for a log law with a shifted origin. *Phys. Fluids* **20**, 101507.
- Spalart, P. & Watmuff, J. 1993 Experimental and numerical study of a turbulent boundary layer with pressure gradients. *J. Fluid Mech.* **249**, 337–371.
- Tanarro, A., Mallor, F., Offermans, N., Peplinski, A., Vinuesa, R. & Schlatter, P. 2020 Enabling adaptive mesh refinement for spectral-element simulations of turbulence around wing sections. *Flow Turb. Comb.* **105**, 415–436.
- Toosi, S., Peplinski, A., Schlatter, P. & Vinuesa, R. 2024 The impact of finite span and wing-tip vortices on a turbulent naca0012 wing. Available at: <https://arxiv.org/abs/2310.10857>.
- Vinuesa, R., Negi, P., Atzori, M., Hanifi, A., Henningson, D. & Schlatter, P. 2018 Turbulent boundary layers around wing sections up to $Re_c = 1,000,000$. *Int. J. Heat Fluid Flow* **72**, 86–99.